Ashall, C and Mazzali, PA

 Extracting high-level information from gamma-ray burst supernova spectra

http://researchonline.ljmu.ac.uk/id/eprint/18080/

Article

For more information please contact researchonline@ljmu.ac.uk

Extracting high-level information from gamma-ray burst supernova spectra

C. Ashall [1]★ and P. A. Mazzali[2,3]

[1]*Department of Physics, Florida State University, Tallahassee, FL 32306, USA*
[2]*Astrophysics Research Institute, Liverpool John Moores University, IC2, Liverpool Science Park, 146 Brownlow Hill, Liverpool L3 5RF, UK*
[3]*Max-Planck-Institut für Astrophysik, Karl-Schwarzschild-Str 1, D-85748 Garching, Germany*

ABSTRACT

Radiation transport codes are often used in astrophysics to construct spectral models. In this work, we demonstrate how producing these models for a time series of data can provide unique information about supernovae (SNe). Unlike previous work, we specifically concentrate on the method for obtaining the best synthetic spectral fits, and the errors associated with the preferred model parameters. We demonstrate how varying the ejecta mass, bolometric luminosity (L_{bol}) and photospheric velocity (v_{ph}), affects the outcome of the synthetic spectra. As an example we analyse the photospheric phase spectra of the GRB-SN 2016jca. It is found that for most epochs (where the afterglow subtraction is small) the error on L_{bol} and v_{ph} was ∼5 per cent. The uncertainty on ejecta mass and E_{kin} was found to be ∼20 per cent, although this can be expected to dramatically decrease if models of nebular phase data can be simultaneously produced. We also demonstrate how varying the elemental abundance in the ejecta can produce better synthetic spectral fits. In the case of SN 2016jca it is found that a decreasing ^{56}Ni abundance as a function of decreasing velocity produces the best-fitting models. This could be the case if the ^{56}Ni was synthesized at the side of the GRB jet, or dredged up from the centre of the explosion. The work presented here can be used as a guideline for future studies on SNe which use the same or similar radiation transfer code.

Key words: radiative transfer – supernovae: general.

1 INTRODUCTION

Radiation transfer codes are frequently used in astrophysics to obtain meaningful insight from observations. These codes usually fall in two categories: (i) those which are used to fit individual observations, these codes are usually not computationally expensive and (ii) and those which are predictive but too computationally expensive to be run for every set of observations.

In time domain astrophysics both types of codes have been thoroughly used to model many different transient sources including: core collapse supernovae (SNe, e.g. Hoflich 1991; Baron et al. 1995; Fisher 2000; Mazzali, Iwamoto & Nomoto 2000; Thomas, Nugent & Meza 2011; Jerkstrand et al. 2012), thermonuclear SNe (e.g. Kasen, Thomas & Nugent 2006; Kromer & Sim 2009; Kerzendorf & Sim 2014; Ashall et al. 2016, 2018; Hoeflich et al. 2017; Goldstein & Kasen 2018), and more recently kilonova (e.g. Tanaka & Hotokezaka 2013; Smartt et al. 2017; Bulla 2019). However, previous work has concentrated on the results obtained from

these models, and often neglected to explain the exact modelling method, fitting procedure or associated errors.

One subset of core collapse SN which have often been spectroscopically modelled are stripped envelope supernovae (SE-SNe). These are end result of massive stars that explode after loosing their H/He shells through wind or binary interaction (e.g. Puls, Vink & Najarro 2008; Eldridge et al. 2013). They spectroscopically come in three classes, Type IIb SNe (SNe IIb) which are H and He rich, Type IIb SNe (SNe Ib) which are H poor but He rich, and Type Ic SNe (SNe Ic) which are deprived of both H and He (Filippenko 1997; Matheson et al. 2001).

A subset of SNe Ic, known as broad line SNe Ic (SN Ic-BL), has very broad features and high specific kinetic energies (E_{kin}), and the most energetic of these events have been known to be associated with X-ray flashes (Mazzali et al. 2006, 2008a; Tanaka et al. 2009) and long gamma-ray bursts (LGRBs, e.g. Galama et al. 1998; Iwamoto et al. 1998; Nakamura et al. 2001; Mazzali et al. 2003; Stanek et al. 2003; Ferrero et al. 2006; Woosley & Bloom 2006; Bufano et al. 2012; Jin et al. 2013; Schulze et al. 2014; Modjaz et al. 2016; Toy et al. 2016; Ashall et al. 2019)

To date there have only been six GRB-SNe, all $z < 0.2$, with a high-quality time series of data which is good enough for

★ E-mail: chris.ashall24@gmail.com

Table 1. Input parameters for the spectral models, the errors are given in parenthesis.

Epoch (rest-frame days)	v_{ph} (km s^{-1})	L_{bol} $\log(L_{bol}/L_\odot)$
3.73	35 000(3500)	8.97(0.1)
5.52	32 000(1600)	9.10(0.05)
8.11	28 500(1425)	9.20(0.02)
10.89	25 000(1250)	9.30(0.02)
14.20	22 000(1100)	9.30(0.02)
15.96	20 500(1025)	9.26(0.02)
18.71	19 000(950)	9.26(0.02)
22.12	17 000(850)	9.20(0.02)
32.65	13 500(675)	9.00(0.02)

spectroscopic modelling (see e.g. Iwamoto et al. 1998; Mazzali et al. 2003, 2006; Deng et al. 2005). However, these papers usually just concentrate on the results and do not have a full detailed explanation of the method, analysis, and errors. Therefore, in this paper we concentrate on this, as an example we use the spectra of SN 2016jca presented in Ashall et al. (2019). We specifically concentrate on the spectra of the SN itself. We start by explaining our modelling technique (Section 2) and method (Section 3), then in Section 4 we discuss our starting parameters, followed by a full error analysis in Section 5, in Section 6 the ^{56}Ni distribution in the ejecta is discussed and finally in Section 7 we summarize the results and how this relates to all similar models.

2 THE CODE

In this work, we model nine spectra of SN 2016jca which were analysed in Ashall et al. (2019), they cover the time range (in rest frame) from 3.7 to 32.65 d past explosion. The spectra have been corrected for a GRB afterglow with a time of break of 13 d past explosion. Table 1 contains the individual epochs (in rest frame) for each spectra, as well as the modelling parameters which will be explained below.

First we will discuss the code used in this analysis. An SN ejecta can be assumed to be in homologous starting a few minutes after explosion. This can be approximated by $r = v_{ph}t_{exp}$, where r is the distance of the photosphere from the centre of the explosion, v_{ph} is the photospheric velocity, and t_{exp} is the time from explosion. Therefore, as time passes deeper and deeper layers of the explosion can be observed.

Here, we use a 1D Monte Carlo radiative transfer code to produce synthetic spectra. The code, which is based on Mazzali & Lucy (1993), Lucy (1999), Mazzali et al. (2000), follows the propagation of photon packets through an SN atmosphere. It has been used for many types of SNe before including SNe Ia (e.g. Ashall et al. 2014, 2016, 2018; Galbany et al. 2019) and SE-SN (e.g. Mazzali et al. 2017; Prentice et al. 2018). The code utilizes the Schuster–Schwarzschild approximation which assumes that the radiative energy is emitted at an inner boundary in the form of a blackbody. For GRB-SN this yields good results due to the amount of material above the photosphere. Furthermore, the approximation does not require in-depth knowledge about the radiation transport below the photosphere.

The photon packets have two fates: they either escape the ejecta or re-enter the photosphere, in a process known as back scattering. The photon packets can undergo Thomson scattering and line absorption in the ejecta. If a packet is absorbed, the downward transition it follows is determined by a photon branching scheme, which allows

florescence (blue to red) and reverse florescence (red to blue) to take place. The code utilizes a modified nebular approximation to treat the excitation/ionization state of the gas, to account for the non-local thermodynamical equilibrium effects caused by the diluted radiation field. There is an iteration between the radiation field and the state of the gas until convergence is achieved. Finally, the formal integral of the radiation field is computed to obtain the spectrum.

When modelling SNe using this technique, the abundances of some elements (O, C, Ca, Mg, S, Si, Ti+Cr, and ^{56}Ni) are directly constrained in the data. Other elements (neon being the most abundant element in this group) are present in explosion models but have no lines in the visible range covered by our data, so their abundances are fiducially assumed to match those of models.

The purpose of the code is to produce optimally fitting synthetic spectra. This is done by varying input parameters, such as the bolometric luminosity (L_{bol}), photospheric velocity (v_{ph}), and abundances (Ab). The code requires an input density profile, which can be scaled at the appropriate time from explosion for each modelled spectra, owing to the homologous expansion of the SN. We discuss the density profiles we have tested below.

We have performed the analysis in 1D as carrying out the analysis in 2D or 3D would have to rely entirely upon explosion models, adding more free parameters, making computations much more expensive, and most likely yield results that would only approximately match the observation, meaning we would most likely not get a more accurate solution. We do note that if we were viewing the event perpendicular to the jet axis we would expect to see a different temperature and elemental abundance distribution than if we were viewing it down the axis of the GRB (Tanaka et al. 2007). Although our results are approximate, they should nevertheless be realistic if one understands the constraints and limitations, as is shown by the fact that we can fit the observations with physically sensible parameters. For example the abundance distributions derived using our radiation transport code for Type Ia SNe (Ashall et al. 2018) yields very similar densities and abundance distributions to those produced from non-local thermodynamic equilibrium radiation hydrodynamical models (Hoeflich et al. 2017).

3 MODELLING METHOD

Our code requires as input a density distribution $\rho(r)$ (radius and velocity are equivalent in an SN's homologously expanding ejecta, only a reference time for the density is required), a luminosity L_{bol}, a photospheric velocity v_{ph}, and a set of abundances. This is clearly a large parameter set. However, parameters are not independent. L_{bol} and v_{ph} combine to determine the temperature $T(r)$. In combination with the abundances, $T(r)$ and $Ab(r)$ determine the excitation and ionization state of the gas. All these in turn determine line and electron opacities. Relativistic zero-order corrections are included. Unlike other codes (e.g. Fisher 2000; Thomas et al. 2011) therefore we cannot arbitrarily change one value and leave all others unaffected. While this makes the problem highly non-linear, it also makes the task of identifying the range of likely optimal values easier. Here, we discuss the procedure we adopted in this particular case.

We began with setting a density distribution. We then established the best values of L_{bol} and v_{ph} at all epochs, and tested their uncertainty. We did this keeping abundances constant as a function of velocity, to avoid introducing too many free parameters. Changing the abundances in the ejecta may also alter the ionization and thermal conditions, due to changes in the opacity and hence the back scattering rate. However, using the same radiation transport
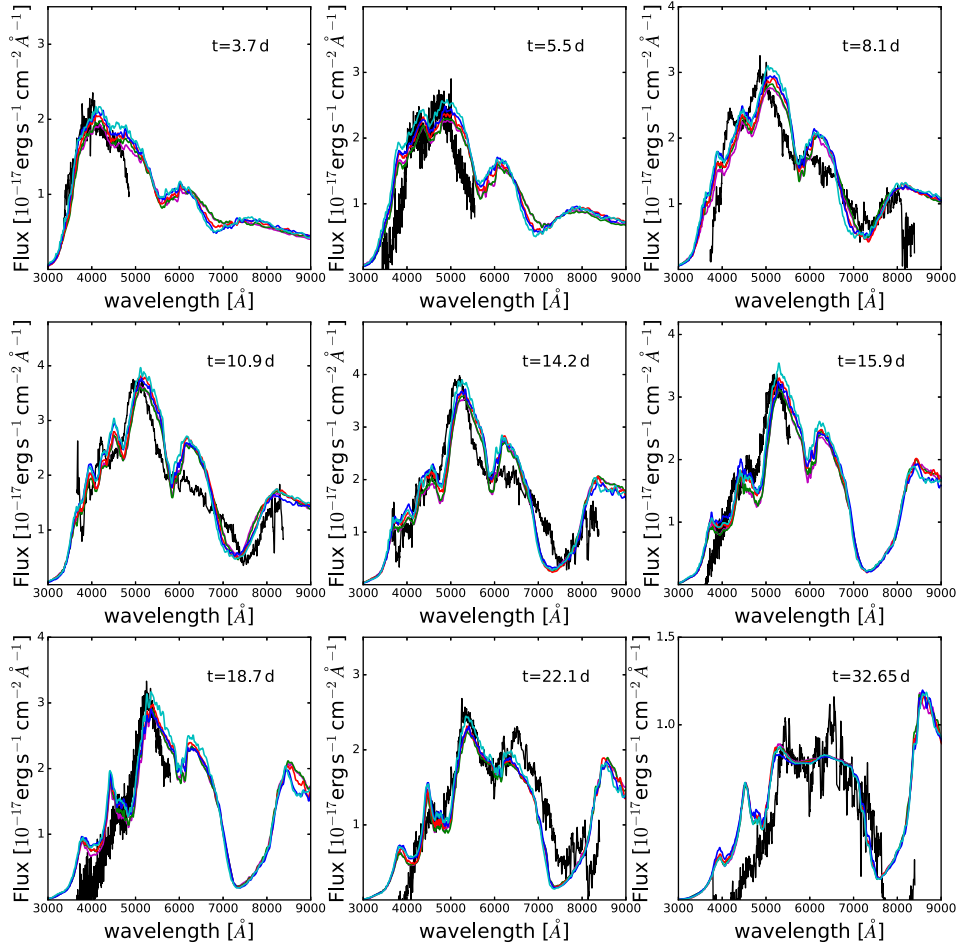
Figure 1. Spectral models produced with five density profiles with the same shape but different masses. The masses of the models are $2\,M_\odot$ (magenta), $4\,M_\odot$ (green), $6.5\,M_\odot$ (red), $8\,M_\odot$ (blue), and $11\,M_\odot$ (cyan). The black spectra are the observations. The different models were produced to conserve $T(r)$. A colour version of this figure is available online.

code, Mazzali et al. (2008b) examined the effects of varying the abundances in the ejecta. They found that the uncertainty on the abundances derived using this method is ∼20 per cent, and that the 'global' parameters L_{bol} and v_{ph} are not significantly affected by changes in the abundances of this magnitude.

4 EXPLOSION DENSITY PROFILE

SN 2016jca has a fairly rapidly evolving light curve compared to other well-studied GRB-SN, which reach peak later. Therefore, to get a first estimate of the combination of E_{kin} and M_{ej}, which produce the light curve and the spectra, we follow the work in Mazzali et al. (2017) and use two well-studied SNe, SN 2006aj, and SN 1998bw, as starting points. SN 2006aj ($M_{ej} = 2\,M_\odot$, $E_{kin} = 1 \times 10^{52}$ erg) (Mazzali et al. 2006) has a similar light curve suggesting the mass may be similar to that of SN 2016jca. Whereas SN 1998bw ($M_{ej} = 10\,M_\odot$, $E_{kin} = 5 \times 10^{52}$ erg) (Iwamoto et al. 1998) has similar spectra suggesting that the E_{kin}/M_{ej} value is similar to SN 2016jca. We consider both the time to peak and the width of the light curve. If we use SN 2006aj as a starting point the two methods of deducing M_{ej} and E_{kin} from the peak time and the light-curve width yield different results, suggesting SN 2006aj is not a good analogue. On the other hand, if we apply the same methodology on SN 1998bw we get in both cases $M_{ej} = 6.5\,M_\odot$, and $E_{kin} = 4 \times 10^{52}$ erg, suggesting

SN 1998bw has the correct E_{kin}/M_{ej} ratio, and SN 2016jca had a smaller mass. Therefore, we use this E_{kin}/M_{ej} value as the basis for the spectral models below.

The explosion model used for SN 1998bw was CO138 (Iwamoto et al. 1998). It is the explosion of the ∼14 $M_\odot$ CO core of a massive star with main-sequence star mass ∼40 $M_\odot$ (Iwamoto et al. 1998). In SN 1998bw, a high isotropic E_{kin} (∼5 × 10^{52} erg) was used to match the observed broad absorption features and to produce the large amount of low-velocity ^{56}Ni typical of SN 1998bw and of all other GRB-SNe. A black hole remnant was assumed, and the inner 3 $M_\odot$ were therefore excised, resulting in an ejecta mass of ∼11 $M_\odot$. In this work, we have used the unaltered hydrodynamic model from Iwamoto et al. (1998). Furthermore, when we scaled the M_{ej} we kept the same E_{kin}/M_{ej} ratio.

Fig. 1 shows models produced with 2, 4, 6.5, 8, and 11 $M_\odot$. The same values of L_{bol} and v_{ph} were used to keep a constant $T(r)$. For all the models the abundances were scaled, at the expense of oxygen and neon with the same proportionally, to keep roughly the same absolute mass of all other elements. Therefore, as the total mass of our ejecta decreases the mass of the heavier elements increases with respect to the light elements (i.e. oxygen and neon). This is counter intuitive and may be uncertain as we get to masses further away from the original explosion model. However, the lowest masses are unlikely to produce a synthetic light curve with the correct
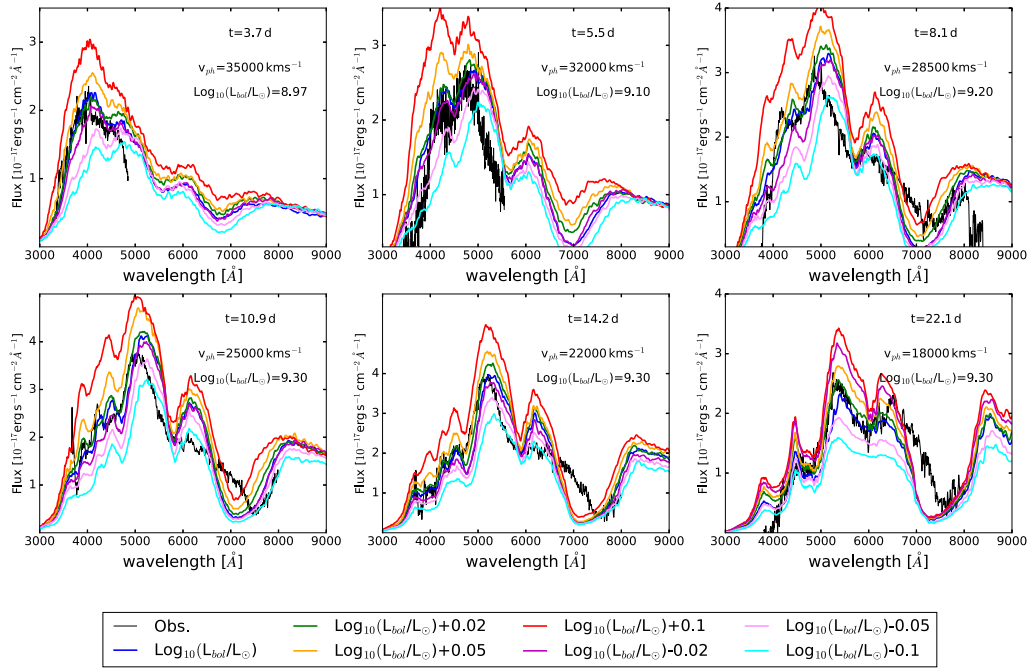
Figure 2. Spectral observations and models of SN 2016jca with varying input luminosities. The blue model is the best-fitting model. A colour version of this figure is available online.

width. It is apparent from the models that there is not enough absorption in the $2\,M_\odot$ model and we can rule it out. Furthermore, the dilution factor, w, in the models should be ~ 0.5. This is only the case for models near $6.5 M_{ej}$, and deviates significantly as the M_{ej} varies away from $6.5 M_{ej}$. Therefore, the $6.5 M_{ej}$ model produced the best results. Combining this with information about the synthetic light-curve model produced below, we take the range of acceptable values as models, and proceed with the $6.5 \pm 1.5\,M_\odot$.

We note we did not test masses below $2\,M_\odot$, as such low masses would not be able to produce the width of the light curve of SN 2016jca. In fact is likely that the $4\,M_\odot$ model would also not be able to reproduce the observed light curve. As discussed below, we produce a model light curve to check our density profile and abundance structure and find good agreement with the our model and observed bolometric light curve.

5 DETERMINING ERRORS

5.1 Bolometric luminosity

As we mentioned above, we used constant abundances throughout the ejecta to determine L_{bol} and v_{ph} at the various epochs and their uncertainty from average models. We use a set of models which have an elemental distribution that reflects the composition of the collapse of a massive stellar carbon–oxygen core as a starting point. Using constant abundances as a function of velocity, for the $M_{ej} = 10\,M_\odot$ model our most abundant elements are O (~ 70 per cent), Ne (~ 20 per cent), and C (~ 7 per cent), followed by Si (~ 1.5 per cent), S (~ 0.5 per cent), and ^{56}Ni (~ 0.4 per cent), with the remaining 0.6 per cent consisting of Mg, Ca, Fe, Ti+Cr. It can be noticed that the ^{56}Ni content far exceeds the Fe abundance. We discuss this in the following sections. This set of model offers a good reproduction of the spectral time series.

To determine the errors, and to explain the fitting procedure, we computed a range of synthetic spectra starting from our main results but varying parameters (L_{bol}, v_{ph}, and ^{56}Ni abundance). We used values of L_{bol} and v_{ph} that yield correct flux levels and spectral distributions, and used abundances that yield reasonably accurate line strength for the most important features.

The error on the bolometric luminosity, was determined by producing models around the best-fitting model, with varying luminosities (see Fig. 2). Changing L_{bol} affects the overall flux, as can be seen in the plot, but also the temperature, such that models with lower L_{bol} are redder, but this only affects the flux region where most photon redistribution occurs, shortwards of 6000 Å. The combination of flux level and spectrum shape is what we used to determine the best model and uncertainties. The plots show that on day 8 and following epochs the error can be estimated as ± 5 per cent, while at earlier times it is larger, close to 10 per cent at day 5. At day 3, the flux is poorly determined, so we use a generous error of 25 per cent.

5.2 Photospheric velocity

Having determined L_{bol} in our models, we now turn to v_{ph}. We produce models around a best-fitting model, with increasing and decreasing values of v_{ph} (see Fig. 3).

As changing v_{ph} does not affect the total flux, the changes in the synthetic spectra are due only to changes in temperature and opacity. The red part of the spectra is largely unaffected, except for a shift of the edges of the broad O I/Ca II absorption caused by the different choices of photospheric velocity.

The fits at 8.1 and 5.5 d begin to become significantly worse when the photospheric velocity is varied by 10 per cent, hence we adopt an error of 5 per cent in v_{ph} at 8.1 and 5.5 d and later epochs. At 3.7 d we adopt an error of 10 per cent as the flux level is more uncertain here, and the shape of the hotter spectra (the one with the lower v_{ph}) matches the shape of the observations well.
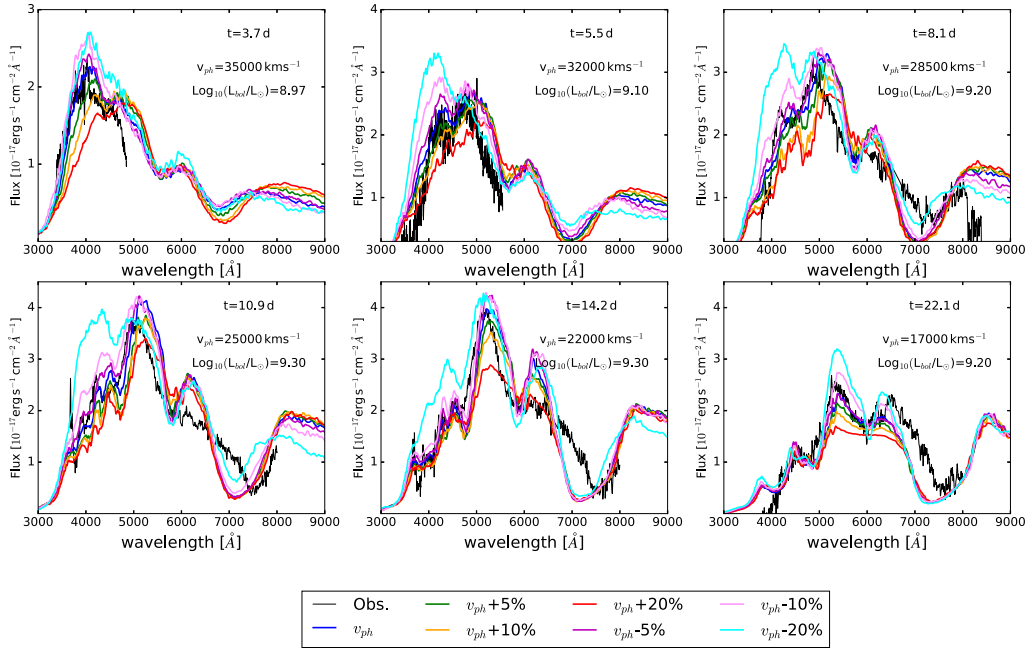
Figure 3. Spectral observations and models of SN 2016jca with varying input photospheric velocities. The blue model is the best-fitting model. A colour version of this figure is available online.

5.3 Bolometric luminosity versus photospheric velocity

As we mentioned above, our input data are not independent. Looking at L_{bol} and v_{ph}, while individual error ranges have been assigned, only combinations of parameters that roughly preserve temperature can keep an ionization and temperature structure similar to the best-fitting model and yield reasonable spectra. Here, we demonstrate that this is the case, combining results with +ve/−ve variations of L_{bol} and v_{ph} around the respective best values. Only values where $\frac{L_{bol}}{v_{ph}^2} \approx$ const reproduce the spectral shape. The set of models thus produced are all similar in shape, except for the differences in line width and strength resulting from using different depths, but the change in L_{bol} causes the overall flux level to deviate, making it easy to discriminate among models and leaving the actual flux calibration of the data as the main uncertainty. This is very useful in constraining the possible range of parameters, see Fig. 4. Therefore, if changing L_{bol} to a larger value, only larger values of v_{ph} are compatible, and vice versa, which reduces the allowed space of parameters.

It is apparent from the models that there is no degeneracy between L_{bol} and v_{ph}, such that varying L_{bol} by 10 per cent and v_{ph} by 5 per cent, even in the same direction, produces significantly worse fits after 5.5 d. At 3.7 d several models yield good fits, hence our errors here are of the order of 20 per cent on L_{bol} and 10 per cent on v_{ph}.

6 DETERMINING THE Ni DISTRIBUTION IN THE OUTER LAYERS

In Type I SNe most of the opacity is usually caused by metal lines, in particular Fe lines. GRB-SNe in general, and SN 2016jca is no exception, are very red at early phases, although they are more luminous on average than other SNe Ic (Prentice et al. 2016). This red colour is often attributed to the high velocities reached in these SNe, but the effect is not simply one of temperature. It is again the result of different line opacities. Here, we show that the early red

colour is due to the presence of ^{56}Ni at high velocities. This makes GRB-SNe different from low-energy SNe Ic, which tend to have blue spectra at early times e.g. SN 1994I (Sauer et al. 2006). First we test the iron abundance. Although it should be expected that the Fe content at early times should reflect that of the progenitor star, and therefore presumably be similar to that of the host galaxy, we ask the question whether the red colour is due to Fe abundance by testing models with varying Fe composition.

Fig. 5 shows synthetic spectra for the time series of spectra of SN 2016jca obtaining for different Fe abundances. These models have been produced using stable Fe abundances, and with no ^{56}Ni, so the Fe content does not change as a function of time. For all spectra at 5.5, 8.1, 10.9 d there is excess flux in the blue part of the spectra. Furthermore, for large Fe abundances strong Fe II lines ($\lambda\lambda$ 4923 5018 5169), which are much deeper than the observations appear in the 4000–5000 Å range. Even for large Fe abundances the blue part of the spectrum is not sufficiently blocked, as there are not enough strong Fe lines in this region. Co and Ni are required to block the excess flux in the blue part of the spectra, and as no stable Co is produced in GRB-SN explosions, high-velocity ^{56}Ni is needed in the models.

As Fe cannot shape the spectra of SN 2016jca, we show here that ^{56}Ni and its decay products offer the correct opacities. We tested the abundances of various elements to verify what causes the spectra to be red, and found that the element that most affects the shape of the spectrum is ^{56}Ni. We show a set of models with different ^{56}Ni abundances and a flat distribution. These clearly show that ^{56}Ni and decay products have a major effect on the spectral shape, especially at early times. More ^{56}Ni suppresses the blue and enhances the redder part of the spectrum by fluorescence, in particular near the *V* band, where line opacity is smaller and photons can escape. We show models computed with different constant initial ^{56}Ni abundances in Fig. 6. It is apparent that the best-fitting ^{56}Ni abundance is 0.4 per cent, the 0.2 per cent model does not have enough UV blocking at day 5.5 or 8.1 and the 0.6 per cent model
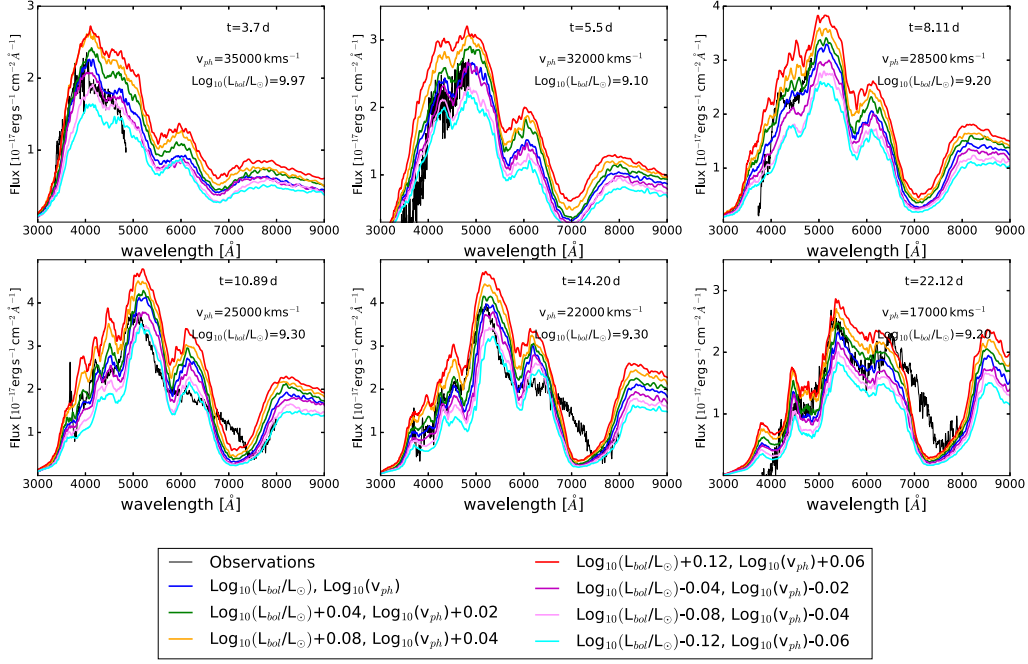
Figure 4. Spectral observations and models of SN 2016jca with varying input luminosities and photospheric velocities, where $\frac{L_{bol}}{v_{ph}^2} \approx$ const. The blue model is the best-fitting model. A colour version of this figure is available online.
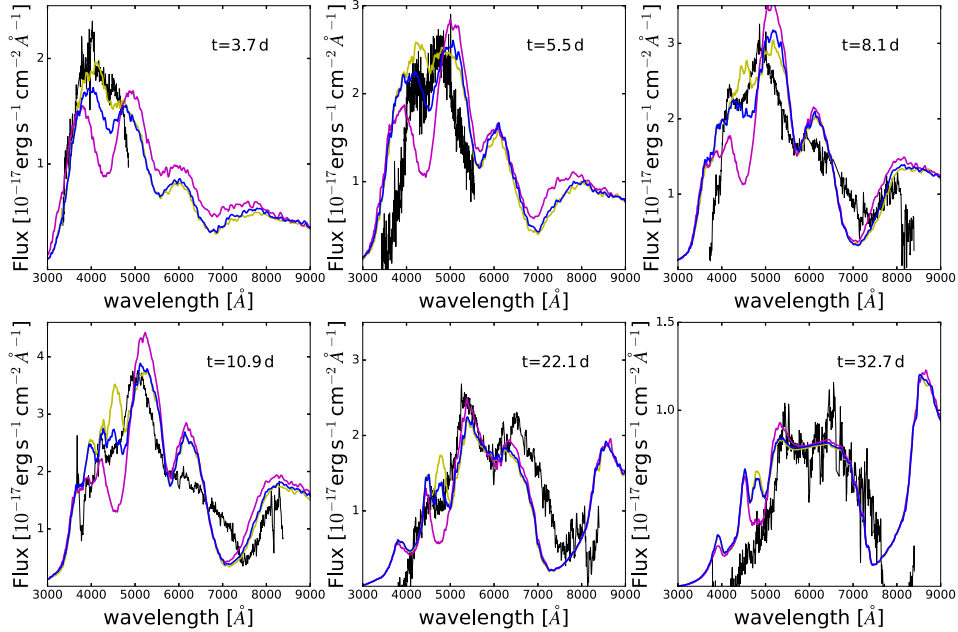

Figure 5. Synthetic spectral models produced with no ^{56}Ni, but different stable Fe mass fractions of 1×10^{-4} (yellow), 1×10^{-5} (blue), 1×10^{-3} (magenta). A colour version of this figure is available online.

has too much Fe absorption (produced from the decay of ^{56}Ni) at later times (e.g. 15.9 and 22.1 d). In fact, the results from Fig. 6 may suggest that at early times (high velocities) there is a large ^{56}Ni abundance which can block the flux in the UV, and at later times (lower velocities) the ^{56}Ni abundance is much less.

Having a constant mass fraction of ^{56}Ni as a function of velocity, is difficult to coincide with an aspherical explosion, especially if the ^{56}Ni is produced on the side of the GRB jet. However, it

could be expected that the ^{56}Ni abundances could decrease as a function of decreasing velocity. This is as the photosphere recedes the jet, heavily synthesized region surrounding the jet, will becomes a smaller overall fraction of the total observed region. Although in the centre of the ejecta the ^{56}Ni abundances would be expected to increase again. To test for this models were produced for both increasing and decreasing ^{56}Ni abundance as a function of velocity, see Fig. 7.
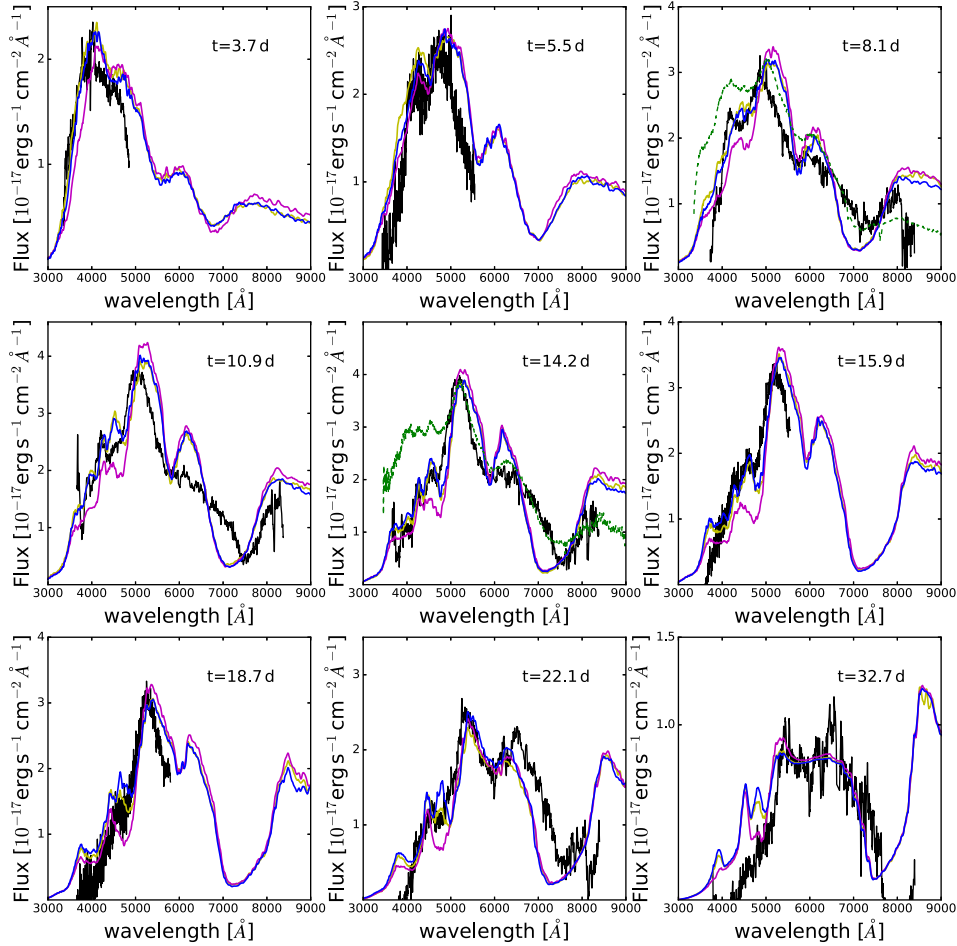
Figure 6. Synthetic spectra produced with varying constant ^{56}Ni abundances. The ^{56}Ni abundances are $\sim$0.4 per cent (blue), $\sim$0.2 per cent (yellow), and $\sim$0.6 per cent (magenta). At 8.1 and 14.2 d, the spectra of SN 1998bw have been plotted (green dashed) normalized to the peak of the SN 2016jca spectra. A colour version of this figure is available online.

The yellow model in which the ^{56}Ni abundance increases as a function of decreasing velocity produces poor fits at both early and late times. At later times (22.12 d) there is too much absorption at $\sim$4200 Å, caused by the decay of ^{56}Ni, and at early times (3.7, 5.5, and 8.1 d). This is as there is not enough blocking by Ni II and Co II lines. The blue models have a constant ^{56}Ni abundance of 0.4 per cent and produce good fits at all epochs. However, the magenta models which have a decreasing ^{56}Ni abundance as a function of decreasing velocity produce fits which are better or as good as the blue models. Therefore, the range of best-fitting lines between the magenta and blue models. This range of ^{56}Ni abundance is shown in Fig. 8 as the shaded region.

The fact that we have a solution where the ^{56}Ni abundance is decreasing as velocity could imply that SN is aspherical both in shape and in elemental distribution. This is as the ^{56}Ni could have been synthesized on the side of the jet. As time passes, the jet, and heavily synthesized material surrounding it, would cover a smaller overall fraction of the total material observed above the photosphere, and more lighter material on the side of the ejecta would be observed. Hence, the metal abundance would decrease at the expense of lighter elements.

Izzo et al. (2019) have also claimed evidence for high-velocity ^{56}Ni in a GRB-SN, they suggest that this could have been produced by a jets and a cocoon breaking through a stellar surface. However, spectral models of the radial dependence of ^{56}Ni were first suggested by the original preprint of Ashall et al. (2019). Both pieces of work use radiation transport codes, however Izzo et al. (2019) use a code based on the one from this work and did not perform an error analysis. They claim that that SN 2017iuk requires a flat density structure in the outer most layers. In this work and in Ashall et al. (2018), it was found that there was no need to enhance the outer density structure in the outer layers for SN 2016jca, and an increase in abundance of Fe-group elements was sufficient. This was not tested by Izzo et al. (2019), and it could in fact be an alternative solution. In the case presented here, blobs of ^{56}Ni could have been dredged up from the centre of the explosion by the jet. However, the need for high-velocity ^{56}Ni may not be required in all SNe, as is seen in Fig. 6, SN 1998bw has more flux in the blue than SN 2016jca. This is likely to be caused by a lack of Fe-group elements at high velocity in the ejecta of SN 1998bw, which could have been due to the even being observed slightly off-axis, hence SN 1998bw had a weak afterglow.

7 BOLOMETRIC LIGHT CURVE

To verify that the results we obtained are realistic we produce a model bolometric light curve of SN 2016jca. The light-curve code
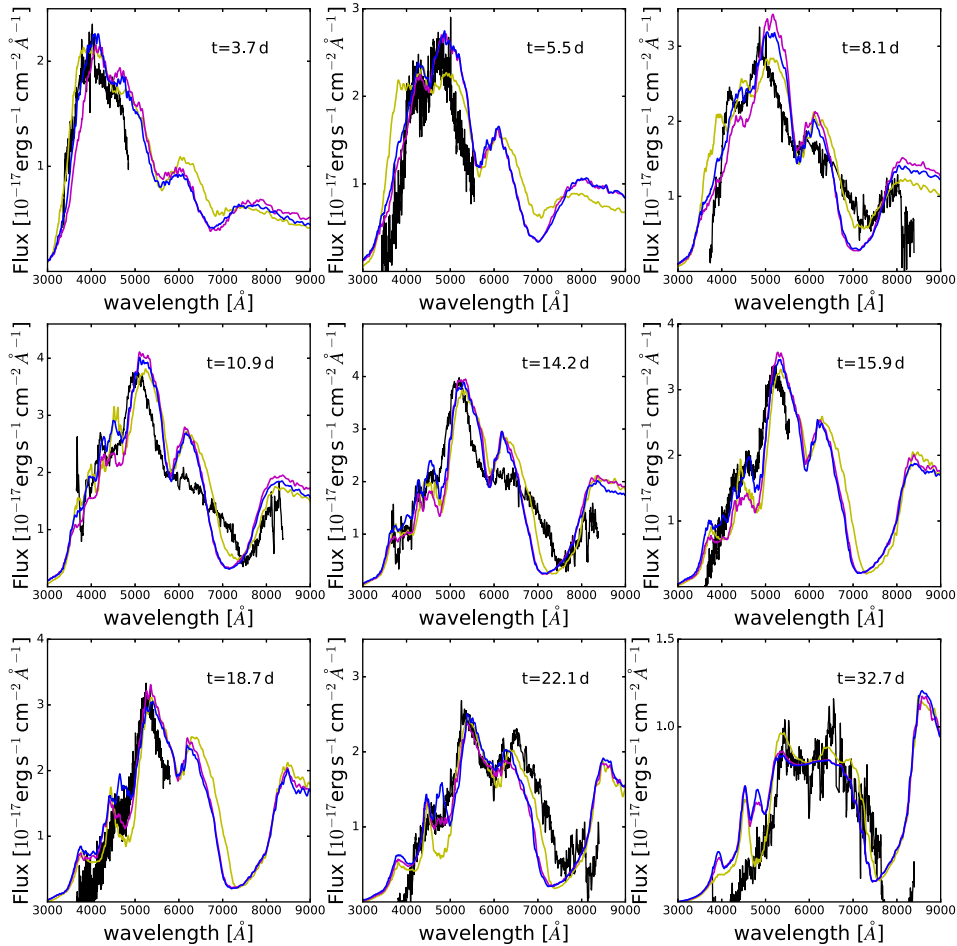
Figure 7. Spectral models produced with ^{56}Ni abundances. The best-fitting blue model has a ^{56}Ni abundance of ∼0.4 per cent, the magenta model has a ^{56}Ni abundance which decreases as velocity decreases, and the yellow model has the opposite trend. Note that a variation of this plot is presented in Ashall et al. (2019). A colour version of this figure is available online.
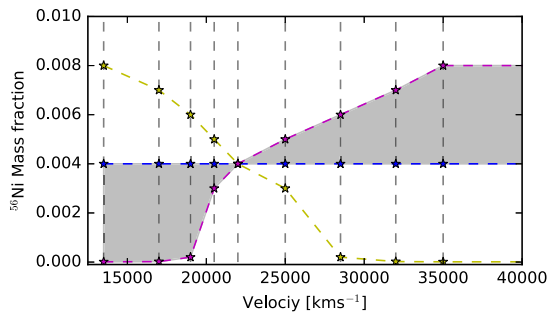

Figure 8. The ^{56}Ni abundance distribution as a function of velocity for the three models presented in Fig. 7. The values of ^{56}Ni which produce good fits are highlighted in grey. The dashed horizontal lines represent the photospheric velocity from the nine spectral models. Note that a variation of this plot is presented in Ashall et al. (2019). A colour version of this figure is available online.

is a Monte Carlo code which was first presented in Cappellaro et al. (1997) and then expanded in Mazzali (2000). In the light-curve models gamma-ray opacity is assumed to be constant and equal to $0.027 \, \mathrm{cm}^2 \, \mathrm{g}^{-1}$ (Sutherland & Wheeler 1984). Positrons are propagated using an opacity of $7 \, \mathrm{cm}^2 \, \mathrm{g}^{-1}$ as an approximation (Sutherland & Wheeler 1984). Optical photons are supposed to

encounter an opacity dominated by line opacity and which therefore depends on composition and slowly decreases with time, as in Hoeflich & Khokhlov (1996) and Mazzali et al. (2001).

With a given density structure and abundance composition the code follows the propagation of photons through the SN atmosphere in the expanding ejecta and a synthetic light curve is produced. The abundance are assumed to be constant below $13 \, 500 \, \mathrm{km \, s}^{-1}$ and the density profile from the hydrodynamical model is used. The bulk of ^{56}Ni is assumed to be centrally located, and the total mass of the ^{56}Ni was taken as $0.27 \, \mathrm{M}_\odot$ as derived from the peak of the bolometric light curve (Ashall et al. 2019). Fig. 9 shows the observed bolometric light curve from Ashall et al. (2019) and the synthetic light curve. The model provides a consistent fit to the observations, which demonstrates that the input density profile, ejecta mass, E_{kin} and ^{56}Ni distribution is consistent with both the spectra and light curves of SN 2016jca.

8 CONCLUSIONS

Analysing the spectra of SN associated with LGRBs is one of the most promising ways to obtain physical information about these rare explosions. However, previous studies have tended to just publish the best-fitting results with little information about the
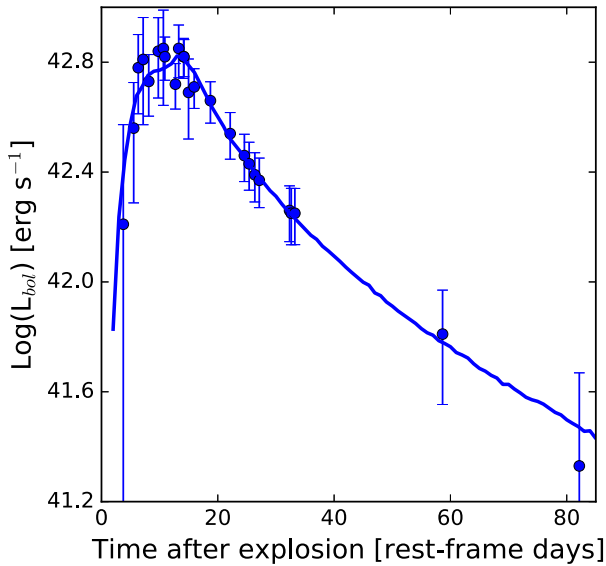
Figure 9. The observed (blue circles) and modelled (blue solid line) bolometric light curves of SN 2016jca. A colour version of this figure is available online.

fitting method, or associated errors. Therefore, in this analysis, we concentrate on the method, errors, and results.

As an example, a high-quality time series of the photospheric phase spectra of SN 2016jca was analysed using a Monte Carlo radiation transport code. It was demonstrated how changes in L_{bol} affects the temperature in the models, as well as the overall flux, where models with lower L_{bol} are redder. This occurs in the flux region where most photon redistribution occurs, shortwards of 6000 Å. Whereas, changing v_{ph} affects the temperature and opacity. For most epochs (where the GRB afterglow is weak) the error in L_{bol} and v_{ph} is 5 per cent.

It was also shown when $\frac{L_{bol}}{v_{ph}^2} \approx$ const spectral fits begin to degrade if parameters are moved away from the best-fitting solutions. Even varying the L_{bol} by 10 per cent and v_{ph} by 5 per cent, so the parameters roughly preserve temperature and can keep a similar ionization and temperature structure, produces worst fits. This demonstrates for a unique set of observations there is only one L_{bol} and v_{ph} which produce good fits.

The effect of vary ejecta mass was also explored. Previous work has examined the slope of the outer density profile and how it affects the broadness of the features (Mazzali et al. 2017). Here, we concentrated on having a constant E_{kin}/M_{ej} but varying the overall M_{ej}. This roughly keeps the spectral shape constant, as long as there is enough mass above the photosphere to form opacity and the absolute mass of the elements which form the lines stays constant between different values of M_{ej}. By modelling only the photospheric phase spectra we found that the errors on M_{ej} were 20 per cent, and because of this so were the errors on E_{kin}. However, for an individual M_{ej} the error on E_{kin} is much smaller (see Mazzali et al. 2017). Furthermore, simultaneous photospheric phase, nebular phase, and bolometric light-curve models would dramatically reduce the error on M_{ej}. In the case of SN 2016jca, the best-fitting density profile was $6.5 \pm 1.5\,M_\odot$, and a E_{kin} of $4 \pm 0.8 \times 10^{52}$ erg ($1–3 \times 10^{52}$ erg when correcting for asphericity; Maeda et al. 2002).

In the modelling procedure, the initial abundances were kept constant and consistent with explosion models. However, as each individual SE-SN is unique it is likely that the abundances are not always the same, which can add a lot more free parameters. Therefore, the method which is used is to varying individual abundances by a constant value for all epochs to see if the fits improve. For our test case, SN 2016jca, the observations demonstrated that there was less flux in the blue part of the spectra compared to previous events, possibly due to increased line blanketing. It was found that increasing the stable Fe abundance did not produce the correct opacity. A time variable opacity was required, and high-velocity ^{56}Ni provided this. However, having a constant ^{56}Ni abundance at high velocities is hard to coincide with explosion models, therefore a decreasing ^{56}Ni abundance as a function of decreasing velocity was also tested, and these models produced marginally better fits to the data. In this scenario, the ^{56}Ni would have been synthesized around the jet as it passed through the stellar surface, or it could have been dredged up from the centre of the star by the jet. Either way as time passes and the photosphere recedes the jet and the high-energy material surrounding it would contribute to less and less over the overall fraction of the observed material. Hence, the ^{56}Ni abundance would decrease as a function of decreasing velocity.

The work presented here has demonstrated how radiation transport models can be used to obtain physics information about SE-SN explosions. We have specifically concentrated on the fitting procedure and the associated errors with them. Although the problem is non-linear it is apparent that only one set of parameters produce the best-fitting synthetic models. This paper can be used as a guideline for future studies which use the same or similar radiation transfer codes.

REFERENCES

Ashall C., Mazzali P., Bersier D., Hachinger S., Phillips M., Percival S., James P., Maguire K., 2014, MNRAS, 445, 4427
Ashall C., Mazzali P. A., Pian E., James P. A., 2016, MNRAS, 463, 1891
Ashall C. et al., 2018, MNRAS, 477, 153
Ashall C. et al., 2019, MNRAS, 487, 5824
Baron E. et al., 1995, ApJ, 441, 170
Bufano F. et al., 2012, ApJ, 753, 67
Bulla M., 2019, MNRAS, 489, 5037
Cappellaro E., Mazzali P. A., Benetti S., Danziger I. J., Turatto M., della Valle M., Patat F., 1997, A&A, 328, 203
Deng J., Tominaga N., Mazzali P. A., Maeda K., Nomoto K., 2005, ApJ, 624, 898
Eldridge J. J., Fraser M., Smartt S. J., Maund J. R., Crockett R. M., 2013, MNRAS, 436, 774
Ferrero P. et al., 2006, A&A, 457, 857
Filippenko A. V., 1997, ARA&A, 35, 309
Fisher A. K., 2000, PhD thesis, The University of Oklahoma
Galama T. J. et al., 1998, Nature, 395, 670
Galbany L. et al., 2019, A&A, 630, A76
Goldstein D. A., Kasen D., 2018, ApJ, 852, L33
Hoeflich P., Khokhlov A., 1996, ApJ, 457, 500
Hoeflich P. et al., 2017, ApJ, 846, 58
Hoflich P., 1991, A&A, 246, 481
Iwamoto K. et al., 1998, Nature, 395, 672
Izzo L. et al., 2019, Nature, 565, 324

Jerkstrand A., Fransson C., Maguire K., Smartt S., Ergon M., Spyromilio J., 2012, A&A, 546, A28

Jin Z.-P. et al., 2013, ApJ, 774, 114

Kasen D., Thomas R. C., Nugent P., 2006, ApJ, 651, 366

Kerzendorf W. E., Sim S. A., 2014, MNRAS, 440, 387

Kromer M., Sim S. A., 2009, MNRAS, 398, 1809

Lucy L. B., 1999, A&A, 345, 211

Maeda K., Nakamura T., Nomoto K., Mazzali P. A., Patat F., Hachisu I., 2002, ApJ, 565, 405

Matheson T., Filippenko A. V., Li W., Leonard D. C., Shields J. C., 2001, AJ, 121, 1648

Mazzali P. A., 2000, A&A, 363, 705

Mazzali P. A., Lucy L. B., 1993, A&A, 279, 447

Mazzali P. A., Iwamoto K., Nomoto K., 2000, ApJ, 545, 407

Mazzali P. A., Nomoto K., Patat F., Maeda K., 2001, ApJ, 559, 1047

Mazzali P. A. et al., 2003, ApJ, 599, L95

Mazzali P. A. et al., 2006, Nature, 442, 1018

Mazzali P. A. et al., 2008a, Science, 321, 1185

Mazzali P. A., Sauer D. N., Pastorello A., Benetti S., Hillebrandt W., 2008b, MNRAS, 386, 1897

Mazzali P. A., Sauer D. N., Pian E., Deng J., Prentice S., Ben Ami S., Taubenberger S., Nomoto K., 2017, MNRAS, 469, 2498

Modjaz M., Liu Y. Q., Bianco F. B., Graur O., 2016, ApJ, 832, 108

Nakamura T., Mazzali P. A., Nomoto K., Iwamoto K., 2001, ApJ, 550, 991

Prentice S. J. et al., 2016, MNRAS, 458, 2973

Prentice S. J. et al., 2018, MNRAS, 478, 4162

Puls J., Vink J. S., Najarro F., 2008, A&AR, 16, 209

Sauer D. N., Mazzali P. A., Deng J., Valenti S., Nomoto K., Filippenko A. V., 2006, MNRAS, 369, 1939

Schulze S. et al., 2014, A&A, 566, A102

Smartt S. J. et al., 2017, Nature, 551, 75

Stanek K. Z. et al., 2003, ApJ, 591, L17

Sutherland P. G., Wheeler J. C., 1984, ApJ, 280, 282

Tanaka M., Hotokezaka K., 2013, ApJ, 775, 113

Tanaka M., Maeda K., Mazzali P. A., Nomoto K., 2007, ApJ, 668, L19

Tanaka M. et al., 2009, ApJ, 700, 1680

Thomas R. C., Nugent P. E., Meza J. C., 2011, PASP, 123, 237

Toy V. L. et al., 2016, ApJ, 818, 79

Woosley S. E., Bloom J. S., 2006, ARA&A, 44, 507

This paper has been typeset from a TEX/LATEX file prepared by the author.